Article

Potassium-Promoted Limestone for Preferential Direct Hydrogenation of Carbonates in Integrated CO_2 Capture and Utilization

Shuzhuang Sun,[†] Zheng Chen,[†] Yikai Xu, Yuanyuan Wang, Yingrui Zhang, Catherine Dejoie, Shaojun Xu,* Xin Xu,* and Chunfei Wu*

ACCESS | Metrics & More | Article Recommendations | SI Supporting Information

ABSTRACT: Integrated CO_2 capture and utilization (ICCU) via the reverse water–gas shift (RWGS) reaction offers a particularly promising route for converting diluted CO_2 into CO using renewable H_2. Current ICCU-RWGS processes typically involve a gas–gas catalytic reaction whose efficiency is inherently limited by the Le Chatelier principle and side reactions. Here, we show a highly efficient ICCU process based on gas–solid carbonate hydrogenation using K promoted CaO (K-CaO) as a dual functional sorbent and catalyst. Importantly, this material allows ~100% CO_2 capture efficiency during carbonation and bypasses the thermodynamic limitations of conventional gas-phase catalytic processes in hydrogenation of ICCU, achieving >95% CO_2-to-CO conversion with ~100% selectivity. We showed that the excellent functionalities of the K-CaO materials arose from the formation of $K_2Ca(CO_3)_2$ bicarbonates with septal K_2CO_3 and $CaCO_3$ layers, which preferentially

K_2CO_3 catalyzes selective direct hydrogenation of $CaCO_3$ via $K_2Ca(CO_3)_2$ intermediate

undergo a direct gas–solid phase carbonates hydrogenation leading to the formation of CO, K_2CO_3 CaO and H_2O. This work highlights the immediate potential of K-CaO as a class of dual-functional material for highly efficient ICCU and provides a new rationale for designing functional materials that could benefit the real-life application of ICCU processes.

KEYWORDS: carbon dioxide, hydrogenation, selectivity, integrated CO_2 capture and utilization, transition-metals free catalysts, reverse water–gas shift reaction, dual functional material
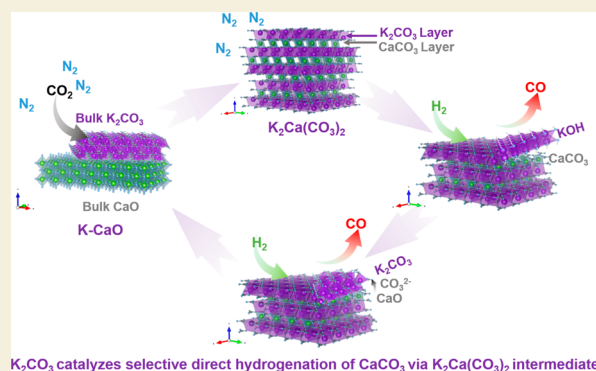
1. INTRODUCTION

The emission of CO_2 from using fossil fuels is a significant contributor to climate change.[1] However, fossil fuels will still play a dominate role as a source of energy in the near future.[2] Although the application of renewable energy (e.g., solar and wind energy) mitigates the challenges related to CO_2 emissions, it faces shortcomings of high cost, low generation efficiency, and slow deployment.[3,4] Consequently, upcycling CO_2 to store renewable energy and keeping it in the carbon cycle provide practical strategies to address the above challenges. To shorten and simplify the whole CO_2 capture and utilization processes, integrated CO_2 capture and utilization (ICCU) processes have been proposed and studied.[5] In a typical ICCU process, CO_2 is first captured and fixed from diluted sources (e.g., flue gas) using sorbents, such as CaO and monoethanolamine.[6,7] Subsequently, the saturated sorbents can be regenerated by converting the adsorbed CO_2 into valuable chemicals, such as CO and CH_4.[8–10] A wide range of catalytic processes have been attempted for the utilization process in ICCU, such as photocatalytic,[11,12] electrocatalytic,[10,13] plasma-catalytic,[14,15]

and thermo-catalytic[9,16,17] processes (Figure 1d). The ICCU can occur under mild conditions (e.g., room temperature) with the assistance of photo- or electrocatalysts, representing a sustainable concept for reducing CO_2 emission. However, they are limited by the low reaction efficiency (Figure 1d) and inhibited by the system complexity in scaling up.[18] Compared to those processes, the conventional thermo-catalytic ICCU under relatively mild conditions presents a more practical solution to meet the urgent industrial level deployment requirement for carbon neutrality in the CO_2 emission point, such as the power plants.[19]

Integrated CO_2 capture and reverse water–gas shift (eq 1) reaction (ICCU-RWGS) is a promising route to reduce CO_2 into CO using renewable H_2. This combined with the
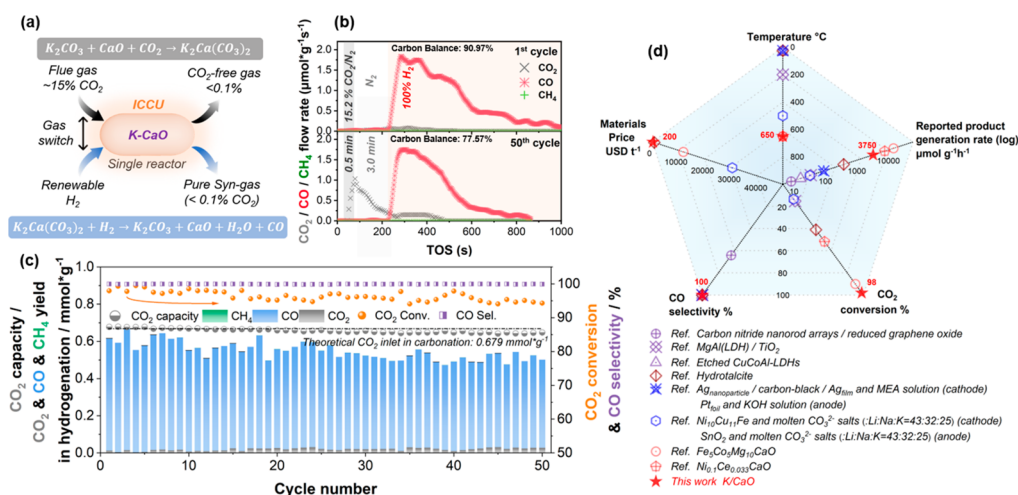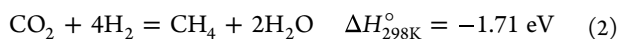
Figure 1. ICCU performances using 20 mol % K-CaO. ICCU schematic diagram and the pivotal reactions using K-promoted CaO (a). The real time (b) and cyclic (c) ICCU performance at 650 °C using 20 mol % K-CaO (carbonation: 15.2% CO_2/N_2 for 0.5 min; purge: N_2 for 3.0 min; hydrogenation: 100% H_2 to the end; carbon balance: C1 species during hydrogenation to CO_2 capacities during carbonation). (d) Comparison of reported integrated CO_2 capture and utilization systems.[9−12,14,16,25,26]

Fischer–Tropsch process, liquid chemicals with long lifetime can be obtained from CO.[20] It was widely believed that the CO_2 is captured in the form of carbonates (eq 3) during CO_2 capture step and then the gaseous CO_2, decomposed from carbonates, react with H_2 on the active sites of the catalysts in an integrated hydrogenation step.[9,16] Hence, many researchers used the experience of catalyst design from conventional RWGS into ICCU-RWGS to enhance its performance.[8,9,16,17] Typically, dual functional materials (DFMs), including active catalytic metals (e.g., Ni or Fe) and adsorbents (e.g., CaO), are widely applied in ICCU.[9,21,22] However, due to the Le Chatelier principle-controlled equilibrium of RWGS and the occurrence of side reactions (e.g., eq 2), the performance of ICCU-RWGS is far from ideal. Furthermore, the introduction of active metals would increase the material cost and cause environmental distress.[23]

$$CO_2 + H_2 = CO + H_2O \quad \Delta H_{298K}^\circ = +0.42 \text{ eV} \quad (1)$$

$$CO_2 + 4H_2 = CH_4 + 2H_2O \quad \Delta H_{298K}^\circ = -1.71 \text{ eV} \quad (2)$$

$$CO_2 + CaO \leftrightarrow CaCO_3 \quad \Delta H_{298K}^\circ = -1.86 \text{ eV} \quad (3)$$

Our previous study confirmed that $CaCO_3$ could directly react with H_2 to generate CO even in the absence of active transition metals (eq 4).[24] However, the inevitable $CaCO_3$ decomposition (reverse eq 3) restricted the CO_2 conversion (<80%) at the regeneration/utilization stage. A significant amount of effort have been made to optimize RWGS catalytic performance, while there have been comparatively fewer studies that reveal the importance of the direct hydrogenation of carbonates. Here we propose a novel strategy to improve the selectivity of direct hydrogenation of carbonates (e.g., eq 4) by hindering the decomposition process (e.g., reverse eq 3), representing a more direct and effective route for CO_2 utilization in ICCU.

$$CaCO_3 + H_2 = CO + CaO + H_2O \quad \Delta H_{298K}^\circ = 2.28 \text{ eV} \quad (4)$$
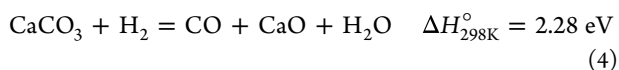
Based on the above understanding, we report a transition-metal-free potassium-promoted CaO (K-CaO) DFM synthesized by a simple impregnation method. By introducing potassium into the commercial CaO, we find that the K species participate in the carbonation of CaO and form stable cocarbonates $K_2Ca(CO_3)_2$ with enhanced reaction kinetics. The generated $K_2Ca(CO_3)_2$ selectively reacts with H_2 rather than decompose to generate CO_2. As a result, we record a CO_2 conversion rate >95% with ∼100% CO selectivity, which outperforms the results of ICCU processes carried out using state-of-the-art active metal (e.g., Ni)-based materials. Combining the experimental characterizations, such as ex-situ synchrotron radiation X-ray diffraction, Raman, and in situ diffused reflectance infrared Fourier transform spectroscopy analysis, with the density functional theory (DFT) calculations, we reveal the key intermediate and mechanism over the K-CaO DFM to facilitate the CO_2 conversion and CO selectivity. Importantly, the K-CaO DFM presented here can be easily produced on a large scale at significantly low capital cost and harmlessly recycled as a cement additive after deactivation, as demonstrated in Figure 1a. This provides a circular solution for large-scale and cost-effective ICCU deployment with a zero-waste approach. Furthermore, this process can potentially be deployed by using two fluidized reactors for continuous CO_2 capture and on-site utilization.

2. RESULTS

The ICCU experiments were carried out in a single tubular fixed-bed reactor (Figure S1), and the carbonation and hydrogenation were realized by switching the inlet gas between simulated flue gas (15.2% CO_2/N_2) and H_2. The K-CaO DFM was obtained by impregnating KNO_3 onto $CaCO_3$ and calcining at 800 °C (Figure S2). During the calcination, the KNO_3 and $CaCO_3$ were thoroughly decomposed and reformed into K_2CO_3, CaO, and $K_2Ca(CO_3)_2$ (fairchildite), respectively (Figure S3 and S4). The commercial CaO reagent was applied as the benchmark material.

As demonstrated in Figure 1b, 20 mol % K-CaO can optimally achieve ca. 100% CO_2 removal efficiency at 650 °C in 0.5 min of the carbonation process. Furthermore, the captured CO_2 (carbonates) can be isothermally converted into CO with sustainable CO_2 conversion (>95%) and CO selectivity (>99.9%) in 50 cycles of ICCU processes (Figure 1c and S5). The uncaptured CO_2 in carbonation slightly
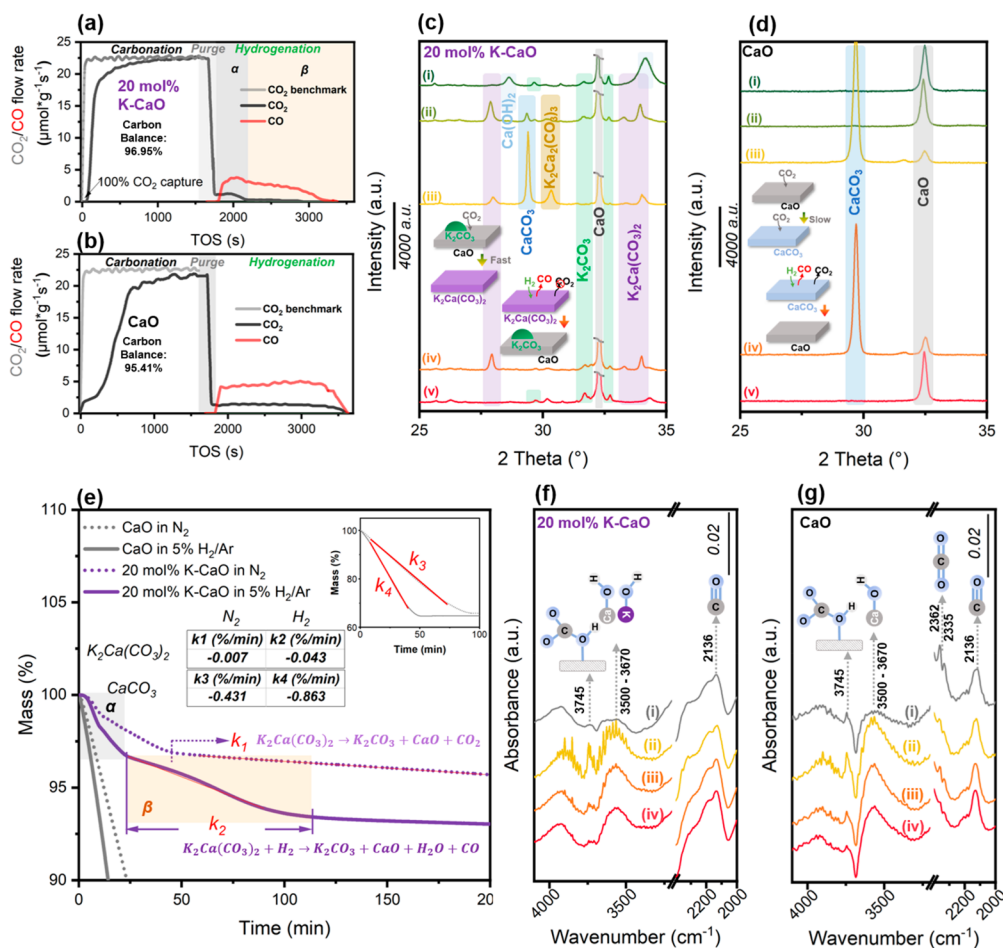
Figure 2. Mechanism investigation of CaO and 20 mol % K-CaO in ICCU. Real time ICCU performance using 20 mol % K-CaO (a) and CaO (b) at 650 °C (carbonation: 15.2% CO_2/N_2 for 30 min; purge: N_2 for 3.0 min; hydrogenation: 100% H_2 to the end; carbon balance: C1 species during hydrogenation to CO_2 capacities during carbonation). (c) Ex-situ SRXRD patterns of 20 mol % K-CaO and (d) ex-situ XRD patterns of CaO in ICCU procedure (i: original material; ii: 0.5 min carbonation; iii: 30 min carbonation; iv: 10 min hydrogenation and v: end of hydrogenation; Note: the 2 Theta = 5° to 80° full patterns are shown in Figures S14 and S15). (e) The mass change of carbonated CaO and 20 mol % K-CaO in N_2 or 5%H_2/Ar at 650 °C (carbonation: 100 mL/min 15.2% CO_2/N_2 for 30 min) and in situ DRIFTs patterns of 20 mol % K-CaO (f) and CaO (g) in the hydrogenation step of ICCU at 650 °C (i: after 30 min carbonation and 10 min Ar purge; ii: 0.5 min hydrogenation; iii: 10 min hydrogenation and v: 60 min hydrogenation).

increases from ~0 to 0.008 mmol g⁻¹ after 50 cycles, while the CO_2 conversion only decreases to 94.3% in cyclic hydrogenation, which outperforms CaO (Figure S5d) and the reported ICCU-RWGS using transition-metal-CaO DFMs[8,9,16] (Table S1) and other ICCUs using photo, electro or plasma-catalytic processes (Figure 1d). Even the molten salt slowly evaporates (Table S2) and the morphologies of materials slightly change in cyclic ICCU evaluations (Figure S13a). However, the main phase composition and surface species are stable (Figures S13b and c), consistent with outstanding performance stability. Notably, the trace transition-metal impurities (i.e., Fe, Pd, etc., in ppm level, reagents might contribute to the presented performance. However, an impact by Fe is unlikely given previous work[8] showing that 10% Fe loading resulted in poorer performance (<85% CO_2 conversion) compared to this work.

In order to demonstrate the superiority of short-term (0.5 min) carbonation and to understand the mechanism, we extended the carbonation time to 30 min. The ICCU performance using 20 mol % K-CaO is displayed in Figure 2a in comparison with the benchmark material of CaO (Figure 2b). Notably, there is an ~1.7 µmol g⁻¹s⁻¹ CO_2 escape flow

using CaO in the initial carbonation stage at 650 °C, which does not occur using 20 mol % K-CaO. Furthermore, the saturated carbonated CaO and 20 mol % K-CaO display vastly different hydrogenation performances. More specifically, the amount of unconverted CO_2 is constant and high (~1.4 µmol g⁻¹s⁻¹) using CaO during the hydrogenation of ICCU at 650 °C (Figure 2b), resulting in a limited CO_2 conversion (~75%, Figure S6). In contrast, there are two hydrogenation stages for 20 mol % K-CaO. The α stage (time on stream, TOS, in the range of 1860−2180 s in Figure 2a) exhibits similar performance with CaO (Figure 2b), while the β stage (TOS of 2180−3300 s in Figure 2a) possesses a low CO_2 flow (<0.2 µmol g⁻¹s⁻¹) and considerable CO flow (~2.6 µmol g⁻¹s⁻¹), resulting in significantly enhanced CO_2 conversion.

The influences of ICCU temperatures and K loadings were also investigated, as shown in Figures S6 and S7. It was found that the temperature was negatively correlated with the CO_2 capture performance. Specifically, CaO could achieve excellent initial CO_2 removal efficiency at 600 °C (Figure S7a, <0.6 µmol g⁻¹ s⁻¹ CO_2 escape rate). However, the CO_2 capture performance of CaO significantly deteriorates at higher temperatures due to the equilibrium of eq 3 (e.g., Figure
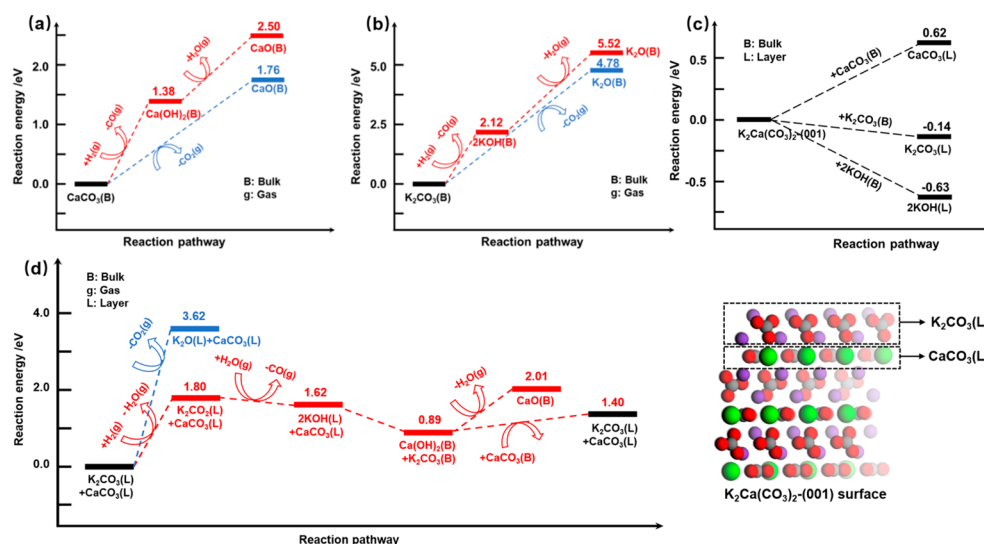
Figure 3. DFT calculations of $CaCO_3$, K_2CO_3, and $K_2Ca(CO_3)_2$ hydrogenation and decomposition. The calculated reaction energies of carbonates direct hydrogenation and decomposition over bulk $CaCO_3$ (a) and bulk K_2CO_3 (b). Formation energies for layers of $CaCO_3$, K_2CO_3, and 2KOH on the $K_2Ca(CO_3)_2$-(001) surface from bulk $CaCO_3$, K_2CO_3, and 2KOH, respectively (c). The calculated reaction energies of carbonates direct hydrogenation and decomposition over layers of $CaCO_3$ and K_2CO_3 on the $K_2Ca(CO_3)_2$-(001) surface (d). The C, O, K, and Ca were presented by the gray, red, purple, and green balls, respectively.

S7c, >5.8 μmol g^{-1} s^{-1} CO_2 escape rate). Notably, higher K loading can effectively improve the CO_2 removal efficiency to 100% in the initial time period of carbonation, even at elevated temperatures. For example, 10 and 20 mol % K-CaO can completely capture CO_2 in the simulated flue gas in the first ~1 min of carbonation at 700 °C (Figure S7c). The high K loading (20 mol %) leads to a slight reduction in the catalyst porosity (Table S2) and CO_2 capture capacity. However, it significantly promoted hydrogenation performance for ICCU. As demonstrated in Figures S8−S10, the unconverted CO_2 released during the hydrogenation stage can be effectively prohibited with higher K loading, while the CO generation rate is only slightly affected. This indicates that the K element might participate in the formation of carbonates during the carbonation step and promote direct hydrogenation of carbonates by inhibiting the generation of CO_2 in the decomposition step subsequent to hydrogenation. Furthermore, the stability of 20 mol % K-CaO is also verified in ICCU with 30 min carbonation condition (Figures S11 and S12).

To reveal the reaction intermediates, ex-situ synchrotron radiation X-ray diffraction (SR-XRD), ex-situ Raman, in situ diffused reflectance infrared Fourier transform spectroscopy (DRIFTs) and powder X-ray diffraction (XRD) were applied to demonstrate the changes to the crystal structure and surface groups of 20 mol % K-CaO at different stages of the ICCU process. The K-CaO samples were selected from five stages during ICCU at 650 °C for ex-situ characterizations, including (i) original as synthesized, (ii) after 0.5 min carbonation, (iii) after 30 min carbonation, (iv) after 10 min hydrogenation, and (v) in the end of hydrogenation, to monitor the evolution of the K-CaO material. The same experiments were also performed with CaO as the benchmark. For the original fresh sample, potassium and calcium mainly exist in the form of K_2CO_3, CaO, $K_2Ca(CO_3)_2$[27,28] (weak intensity), and Ca-(OH)$_2$ (Figures 2c and S14). After 0.5 min of carbonation, the signal intensity for $K_2Ca(CO_3)_2$ significantly increases which is accompanied by the consumption of K_2CO_3 (eq 5), confirming the direct participation of K species in carbonates generation.

There is a trace amount of $CaCO_3$ generation on 20 mol % K-CaO in 0.5 min carbonation, consistent with Raman observation (Figure S15 and Table S3, weak CO_3^{2-} bands at 711 and 1079 cm^{-1}).[29] As a benchmark, the CaO sample showed weak $CaCO_3$ XRD peaks after 0.5 min of carbonation (Figures 2d and S16), indicating the slow kinetics of carbonation of CaO (eq 3). $K_2Ca(CO_3)_2$ is identified as the key species for the 100% CO_2 removal efficiency (Figure 2a and S7) during the carbonation using 20 mol % K-CaO. The as-formed $K_2Ca(CO_3)_2$ might detach from the surface of CaO due to inappropriate crystal structure (Figure S17), and the continuous exposure of CaO contributes to the enhanced CO_2 capture. The sufficient carbonation (30 min) then further promotes the formation of $K_2Ca(CO_3)_2$ (Figures 2c, S14, and S15), accompanied by the enhanced generation of $CaCO_3$. Furthermore, $K_2Ca(CO_3)_2$ can partly form $K_2Ca_2(CO_3)_3$ by combing with $CaCO_3$ (eq 6).

$$K_2CO_3 + CaO + CO_2 = K_2Ca(CO_3)_2 \qquad (5)$$

$$K_2Ca(CO_3)_2 + CaCO_3 = K_2Ca_2(CO_3)_3 \qquad (6)$$

After 10 min of hydrogenation (at the β stage in Figure 2a), the 20% K-CaO material presents mainly three crystal phases which can be attributed to $K_2Ca(CO_3)_2$, K_2CO_3, and CaO (Figures 2c and S14). It is noted that the consumption of $K_2Ca_2(CO_3)_3$ and $CaCO_3$ in the hydrogenation process is fast, which is responsible for the unreacted release of CO_2 in the initial time of hydrogenation (α stage in Figure 2a). In contrast, $K_2Ca(CO_3)_2$ tends to directly react with H_2 to generate CO (eq 7) rather than self-decomposition to generate gaseous CO_2 (eq 8), which is further evidenced by in situ DRIFTS (Figure 2f, no distinct CO_2 generation). Importantly, by the end of the hydrogenation process, the CO_2 saturated 20 mol % K-CaO catalyst is completely regenerated to the initial state (K_2CO_3 + CaO) (Figures 2c and S14) and ready for the next ICCU cycle.

The consumption of carbonates in H_2 atmosphere includes decomposition (reverse eq 3 or eq 8) and direct hydrogenation

(eq 4 or eq 7) pathways, which could be illustrated by the isothermal thermogravimetric analysis under a N_2 or H_2 reducing atmosphere (Figure 2e). Consuming carbonate selectively through direct hydrogenation instead of decomposition is a widely overlooked but highly effective way to achieve a high CO_2 conversion during the hydrogenation stage. It was found that the consumption rate of $K_2Ca(CO_3)_2$ in 5% H_2/Ar (eq 7, k_2) was ~6.1 times faster than its decomposition in N_2 (eq 8, k_1), while the consumption rate of $CaCO_3$ was only 2.0 times faster in 5% H_2/Ar than in N_2. Compared to $CaCO_3$, $K_2Ca(CO_3)_2$ tends to be consumed via direct hydrogenation (eq 7) instead of decomposition (eq 8) in H_2, indicating the high selectivity of direct hydrogenation of $K_2Ca(CO_3)_2$. In short, as illustrated in Figure S18, $K_2Ca(CO_3)_2$ is the key contributor to the 100% CO_2 removal efficiency during carbonation due to the enhanced formation kinetics and also the enhanced CO_2 conversion during hydrogenation via selectively converting carbonates through direct hydrogenation to produce CO (eq 7).

$$K_2Ca(CO_3)_2 + H_2 = K_2CO_3 + CaO + H_2O + CO \tag{7}$$

$$K_2Ca(CO_3)_2 = K_2CO_3 + CaO + CO_2 \tag{8}$$
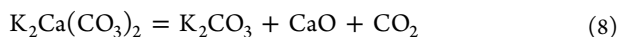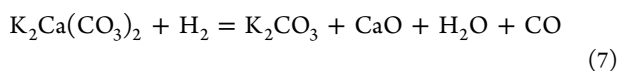
To further study how K promotes the direct hydrogenation of carbonates to CO, DFT calculations were performed to compare the hydrogenation pathway with the decomposition pathway over $CaCO_3$, K_2CO_3, and $K_2Ca(CO_3)_2$, respectively. Since the reaction temperature was relatively high, we assumed that the calculated reaction energies provided a good estimation to compare the preferences of different reaction pathways. As shown in Figure 3a, the $CaCO_3$ hydrogenation possessed a reaction energy of 1.38 eV to release CO and to form $Ca(OH)_2$, which was actually observed in the in situ DRIFTs experiment (Figure 2g). The latter could decompose to ($CaO + H_2O$) easily, as indicated by a further 1.12 eV decomposition energy. Even though the $CaCO_3$ direct decomposition to ($CaO + CO_2$) possessed a higher reaction energy of 1.76 eV, the difference was not high enough to avoid the $CaCO_3$ direct decomposition in opposition to hydrogenation. These calculation results are consistent with the experimental observations that the hydrogenation rate of carbonates to release CO was higher than the rate of decomposition of $CaCO_3$ (Figure 2e) which led to considerable CO_2 release (Figure 2b), albeit with reasonable selectivity. Unlike bulk $CaCO_3$, bulk K_2CO_3 was too stable to decompose, as indicated by a significantly higher calculated reaction energy of 4.78 eV (Figure 3b). In addition, the calculated reaction energy for K_2CO_3 hydrogenation to 2KOH was also quite high, at 2.12 eV, followed by an even higher dehydration reaction energy of 3.40 eV. Thus, neither decomposition nor hydrogenation of bulk K_2CO_3 was feasible, which was consistent with experimental observations performed by using bulk K_2CO_3 (Figure S19).

For the K-promoted CaO system, $K_2Ca(CO_3)_2$ was found to form, consisting of interstitial layers (L) of $CaCO_3$ and K_2CO_3 along the (001) direction (Figure S17). Our DFT calculations showed that the formation energy of K_2CO_3(L) and $CaCO_3$(L) on the $K_2Ca(CO_3)_2$-(001) surface from the bulk materials of K_2CO_3 and $CaCO_3$ are −0.14 and 0.62 eV, respectively (Figure 3c). Thus, more stable K_2CO_3(L) was expected to be formed on the surface. Similar to bulk K_2CO_3, decomposition of K_2CO_3(L) was also unfavored, since the

calculated reaction energy was 3.62 eV (Figure 3d). Meanwhile, the decomposition of nonpreferentially exposed $CaCO_3$ (L) was found to be even more difficult (Figure S20). On the other hand, it was found that the hydrogenation of K_2CO_3(L) to the K_2CO_2(L) intermediate possessed a much lower reaction energy (1.80 eV, Figure 3d). Further hydrogenation resulted in 2KOH (L) with a formation energy of 1.62 eV with respect to K_2CO_3(L), although it was 0.24 eV higher than that of the $CaCO_3$ hydrogenation to $Ca(OH)_2$ (Figure 3a). These calculation results were consistent with the experimental observations that the K-promoted system had a high CO_2 conversion to CO with ignorable CO_2 emission (Figure 2a), although the hydrogenation rate was slower than that of bulk $CaCO_3$. More importantly, although the KOH layer was found to be too stable to be decomposed, it could quickly react with $CaCO_3$(L) with a reaction energy of −0.73 eV to form bulk $Ca(OH)_2$ and K_2CO_3. The as-formed $Ca(OH)_2$ (B) could decompose to generate CaO easily, while bulk K_2CO_3 could react with bulk $CaCO_3$ to regenerate K_2CO_3(L) and $CaCO_3$(L) with a reaction energy of 0.51 eV (Figure 3d). Therefore, DFT calculations suggested that the overall reaction pathway over the K-promoted CaO system involved hydrogenation of K_2CO_3 (L) to produce CO and an intermediate KOH layer on the surface of $CaCO_3$ (L). Simultaneously, a new K_2CO_3 layer was expected to form on the surface of $CaCO_3$ (L). The K_2CO_3 layer possesses superior selectivity to direct hydrogenation instead of decomposition and hence contributes to the excellent CO_2 conversion in ICCU-RWGS using K-promoted CaO DFM.

3. DISCUSSION

The ICCU process based on reverse water−gas shift (RWGS) reaction allows CO_2 to be captured directly from flue gas and converted in situ into highly concentrated and valuable syngas. This provides a novel and promising engineering solution for achieving carbon neutrality. Although ICCU could achieve higher CO_2 conversion rates compared to conventional RWGS, it is still restricted by the equilibrium of RWGS. A 20 mol % K-CaO DFM was produced here, exhibiting cyclically sustainable ~100% CO_2 removal efficiency from the flue gas and >95% CO_2 conversion and ~100% CO selectivity in hydrogenation at 650 °C over 50 reaction cycles, which outperforms the state-of-art counterparts. The performance evaluation, characterization, and simulation reveal that the direct gas−solid carbonates hydrogenation dominates in ICCU using K-CaO DFM, while the carbonates decomposition is highly suppressed due to the mainly formed $K_2Ca(CO_3)_2$ with septal K_2CO_3 and $CaCO_3$ layers. By improving the selectivity of carbonates direct hydrogenation out of decomposition, the ICCU using K-CaO DFM can bypass the gas−gas phase equilibrium restriction of RWGS, producing high purity syngas for the following applications. This work points out the immense potential of carbonate direct hydrogenation via a gas−solid phase CO_2 conversion pathway in ICCU. Moreover, we show that unwanted side reactions such as the decomposition of carbonates can be hindered by introducing K to form intercalated $CaCO_3$ bicarbonate layers. The process shown in this work represents a simple and effective strategy for future materials design in ICCU, which is significant for the deployment of ICCU technologies in real-life settings. More broadly, this work provides an alternative route for enhancing the catalytic efficiency of gas−gas phase reactions, which have significant

implications for many other applications in sustainability beyond ICCU.

4. METHODS

4.1. Material Preparation

The potassium-promoted CaO was prepared by wet impregnation with various molar ratios of potassium to calcium. Typically, as illustrated in Figure S2, x mol KNO$_3$ ($0 < x < 0.1$; Sigma-Aldrich, >99%) was dissolved in 20 mL distilled water, followed by adding $0.1 - x$ mol CaCO$_3$ (Sigma-Aldrich, >99%) into the aqueous solution. The mixture was stirred at room temperature for 1 h and vapored at 90 °C with continuous stirring and then dried at 110 °C overnight. The dried sample was ground and calcined at 800 °C for 5 h at a heating rate of 5 °C min^{-1}. The obtained sample was named as X mol % K-CaO ($X = 1000x$, i.e., $x = 0.01$ for 10 mol % K-CaO).

4.2. Material Characterization

The K loading and Ca content were measured by inductively coupled plasma-optical emission spectroscopy (ICP-OES) using nitric acid digestion. The crystal structures of the materials were tested by powder X-ray diffraction (XRD) on a PANalytical empyrean series 2 diffractometer with a Cu Ka X-ray source. The attenuated total reflectance-Fourier transform infrared spectroscopy (ATR-FTIR) data were collected using Agilent Cary 630. The Raman spectra were characterized on the WITec Alpha 300R Confocal Raman Microscope equipped with a 532 nm diode laser (50 mW). The isothermal thermogravimetric analysis was carried out on a Hi-Res TGA 2950. High-res PXRD of the powder was carried out at beamline ID22 of the European Synchrotron Research Facility (ESRF) at Grenoble, France. The sample was packed into a 0.7 mm capillary that was sealed and mounted on a brass spinner. The sample was attached to a goniometer head and aligned to the beam spot. The diffraction pattern was collected at a wavelength of 0.3542 Å, while the capillary was in the rock mode. The textual information was collected by scanning electron microscopy (SEM) images coupled with an energy dispersive X-ray spectrometer (EDX) on FEI Quanta FEG. The surface area and pore structure of the materials were characterized by an ASAP 3000 analyzer, and the Brunauer−Emmett−Teller (BET) method was used to calculate the surface area. The in situ diffused reflectance infrared Fourier transform spectroscopy (in situ DRIFTs) experiments were carried out using an Agilent Cary 680 FTIR spectrometer with a liquid N$_2$ cooled detector.

4.3. Performance Evaluation and Investigation

The ICCU was carried out in a quartz fixed bed reactor. The quartz reaction tube (12 mm OD; 10.5 mm ID and 650 mm length) was fixed in a tube furnace (Elite), and 0.5 g of sample was placed in the middle of the reaction tube and fixed with quartz wool. The mass of sample loading was calibrated by thermogravimetric analysis with 850 °C N$_2$ calcination to eliminate the mass changes caused by the adsorption of substances in the air. The ICCU evaluation was isothermally carried out under 600, 650, and 700 °C, respectively. The real time gas concentration (CO$_2$, CO, and CH$_4$) during ICCU was monitored by an online gas analyzer (KANE AUTOplus 5−2) equipped with a nondispersive Infrared (NDIR) sensor. 15.2% CO$_2$/N$_2$ and 100% H$_2$ were applied to simulate the flue gas and reducing agent for carbonation and hydrogenation, respectively. Typically, 100 mL min^{-1} (controlled by mass flow meter; OMEGA FMA-A2000) 15.3% CO$_2$/N$_2$ was introduced into the reaction tube for 30 min to demonstrate the CO$_2$ capture procedure, then 100 mL min^{-1} N$_2$ was introduced for 3 min to purge the residual gaseous CO$_2$ followed by switching into 100 mL min^{-1} 100% H$_2$ to achieve the CO generation and regeneration of sorbent. The CO$_2$ conversion, CO selectivity and CO yield in hydrogenation were calculated by integrating the real-time data during hydrogenation, as shown in the following equations:

$$X \ (\mu mol \ s^{-1} \ g^{-1}) = \frac{x \ (\%) \times 1.667 \ (mL \ s^{-1})}{0.0224 \ (mL \ \mu mol^{-1}) \times 0.5 \ (g)} \quad (9)$$

$$C_{CO_2} = \frac{\int (CO + CH_4)}{\int (CO + CH_4 + CO_2)} \times \% \quad (10)$$

$$S_{CO} = \frac{\int CO}{\int (CO + CH_4)} \times \% \quad (11)$$

$$Y_{CO} = \int CO \quad (12)$$

X (μmol s^{-1} g^{-1}; X = CO$_2$, CO or CH$_4$) represents the real-time flow rate of various fraction calculated from the percent fraction data. C_{CO_2} (%), S_{CO} (%), and Y_{CO} (mmol g^{-1}) represent the CO$_2$ conversion, CO selectivity, and CO yield.

4.4. Computational Details

All DFT calculations were performed with Vienna *ab initio* simulation package (VASP).[30,31] The kinetic energy cutoff for the plane wave basis sets of the valence electrons was set to 400 eV. The core electrons were described by the projector augmented-wave (PAW) method.[32] The surface Monkhorst−Pack meshes[33] of $5 \times 5 \times 5$ and $2 \times 2 \times 1$ k-point sampling in the surface Brillouin zone were employed for the bulk and slab model, respectively. For bulk calculations, all atoms were relaxed, and the lattice constants were optimized. For surface slab modeling, the three bottom atomic layers were fixed while the other atomic layers were relaxed. After the convergence criteria for optimizations were met, the largest remaining force on each atom was less than 0.02 eV Å^{-1}. For all calculations, the generalized gradient approximation (GGA) of the Perdew−Burke−Ernzerhof (PBE) functional[34] was used. The contributions of dispersive interactions were accounted for by using the DFT+D3 method with Becke−Johnson (BJ) damping.[35,36] The electronic energy was used for reaction energy calculations, which provided reaction energies of CaCO$_3$ decomposition to produce CO$_2$ (1.76 eV) and overall hydrogenation to produce CO and CaO (B) (2.50 eV) comparable to the experimental enthalpies presented in eq 3 (1.86 eV) and eq 4 (2.28 eV).

For calculating the formation energy of the K$_2$CO$_3$ layer and the KOH layer, the K$_2$Ca(CO$_3$)$_2$-(001) surface with the CaCO$_3$ layer ((001)-CaT) as the terminal layer was used. For calculating the formation energy of the CaCO$_3$ layer, the K$_2$Ca(CO$_3$)$_2$-(001) surface with the K$_2$CO$_3$ layer ((001)-KT) as the terminal was used. Using the K$_2$CO$_3$ layer as an example, the formation energy, $\Delta E_f[K_2CO_3(L)]$, was calculated by

$$\Delta E_f[K_2CO_3(L)] = (E[nK_2CO_3(L)@(001) - CaT]$$
$$- E[nK_2CO_3(B)] - E[(001) - CaT])/n \quad (13)$$

where n represents the number of K$_2$CO$_3$ molecules loaded on the K$_2$Ca(CO$_3$)$_2$-(001) surface, $E[nK_2CO_3(B)]$ is n times of the total energy of bulk K$_2$CO$_3$, $E[(001) - CaT]$ is the total energy of the K$_2$Ca(CO$_3$)$_2$-(001) surface with the CaCO$_3$ layer as terminal, and $E[nK_2CO_3(B)@(001) - CaT]$ is the total energy of n K$_2$CO$_3$ loaded on the K$_2$Ca(CO$_3$)$_2$-(001) surface with the CaCO$_3$ layer as terminal.

■ ASSOCIATED CONTENT

ⓈⒾ Supporting Information

The Supporting Information is available free of charge at https://pubs.acs.org/doi/10.1021/jacsau.3c00403.

Additional experimental details, materials characterizations, detailed data evaluation, and spectral assignment reference (PDF)

■ AUTHOR INFORMATION

Corresponding Authors

Shaojun Xu − *Department of Chemical Engineering, University of Manchester, Manchester M13 9PL, U.K.; UK Catalysis Hub, Didcot OX11 0FA, U.K.;* orcid.org/0000-0002-8026-8714; Email: xus25@cardiff.ac.uk

Xin Xu − *Department of Chemistry, Fudan University, Shanghai 200433, China;* orcid.org/0000-0002-5247-2937; Email: xxchem@fudan.edu.cn

Chunfei Wu − *School of Chemistry and Chemical Engineering, Queen's University Belfast, Belfast BT7 1NN, U.K.;* orcid.org/0000-0001-7961-1186; Email: c.wu@qub.ac.uk

Authors

Shuzhuang Sun − *School of Chemical Engineering, Zhengzhou University, Zhengzhou 450001, China; School of Chemistry and Chemical Engineering, Queen's University Belfast, Belfast BT7 1NN, U.K.*

Zheng Chen − *Department of Chemistry, Fudan University, Shanghai 200433, China*

Yikai Xu − *School of Chemistry and Chemical Engineering, Queen's University Belfast, Belfast BT7 1NN, U.K.; Key Laboratory for Advanced Materials and Feringa Nobel Prize Scientist Joint Research Center, Frontiers Science Center for Materiobiology and Dynamic Chemistry, School of Chemistry and Molecular Engineering, East China University of Science and Technology, Shanghai 200237, China;* orcid.org/0000-0003-3881-8871

Yuanyuan Wang − *School of Chemistry and Chemical Engineering, Queen's University Belfast, Belfast BT7 1NN, U.K.*

Yingrui Zhang − *School of Chemistry and Chemical Engineering, Queen's University Belfast, Belfast BT7 1NN, U.K.*

Catherine Dejoie − *European Synchrotron Radiation Facility, Grenoble 38043, France;* orcid.org/0000-0003-3313-3515

Complete contact information is available at:
https://pubs.acs.org/10.1021/jacsau.3c00403

Author Contributions

†These authors contributed equally to this work. CRediT: **Shuzhuang Sun** conceptualization, data curation, formal analysis, investigation, methodology, writing-original draft, writing-review & editing; **Zheng Chen** conceptualization, data curation, formal analysis, investigation, methodology, writing-original draft, writing-review & editing; **Yikai Xu** conceptualization, supervision, writing-review & editing; **Yuanyuan Wang** data curation, formal analysis, investigation, methodology; **Yingrui Zhang** data curation, formal analysis, investigation, methodology; **Catherine Dejoie** data curation, formal analysis, investigation, methodology, resources, software; **Shaojun Xu** conceptualization, data curation, formal analysis, investigation, methodology, supervision, writing-original draft, writing-review & editing; **Xin Xu** conceptualization, resources, supervision, writing-review & editing; **Chunfei Wu** conceptualization, formal analysis, investigation, project administration, resources, supervision, validation, writing-original draft, writing-review & editing.

Notes

The authors declare no competing financial interest.

■ ACKNOWLEDGMENTS

■ REFERENCES

(1) Lackner, K. S. A guide to CO_2 sequestration. *Science* **2003**, *300* (5626), 1677−1678.

(2) Zou, C.; Zhao, Q.; Zhang, G.; Xiong, B. Energy revolution: From a fossil energy era to a new energy era. *Natural Gas Industry B* **2016**, *3* (1), 1−11.

(3) Moriarty, P.; Honnery, D. Can renewable energy power the future? *Energy Policy* **2016**, *93*, 3−7.

(4) Trainer, T. Some problems in storing renewable energy. *Energy Policy* **2017**, *110*, 386−393.

(5) Duyar, M. S.; Trevino, M. A. A.; Farrauto, R. J. Dual function materials for CO_2 capture and conversion using renewable H_2. *Appl. Catal. B: Environmental* **2015**, *168*, 370−376.

(6) Hanak, D. P.; Anthony, E. J.; Manovic, V. A review of developments in pilot-plant testing and modelling of calcium looping process for CO_2 capture from power generation systems. *Energy Environ. Sci.* **2015**, *8* (8), 2199−2249.

(7) Shao, B.; Zhang, Y.; Sun, Z.; Li, J.; Gao, Z.; Xie, Z.; Hu, J.; Liu, H. CO_2 capture and in-situ conversion: Recent progresses and perspectives. *Green Chemical Engineering* **2022**, *3* (3), 189−198.

(8) Sun, S.; He, S.; Wu, C. Ni promoted Fe-CaO dual functional materials for calcium chemical dual looping. *Chem. Eng. J.* **2022**, *441*, 135752.

(9) Sun, H.; Wang, J.; Zhao, J.; Shen, B.; Shi, J.; Huang, J.; Wu, C. Dual functional catalytic materials of Ni over Ce-modified CaO sorbents for integrated CO_2 capture and conversion. *Appl. Catal. B: Environmental* **2019**, *244*, 63−75.

(10) Lee, G.; Li, Y. C.; Kim, J.-Y.; Peng, T.; Nam, D.-H.; Sedighian Rasouli, A.; Li, F.; Luo, M.; Ip, A. H.; Joo, Y.-C.; Sargent, E. H. Electrochemical upgrade of CO_2 from amine capture solution. *Nature Energy* **2021**, *6* (1), 46−53.

(11) Xia, Y.; Tian, Z.; Heil, T.; Meng, A.; Cheng, B.; Cao, S.; Yu, J.; Antonietti, M. Highly selective CO_2 capture and its direct photochemical conversion on ordered 2D/1D heterojunctions. *Joule* **2019**, *3* (11), 2792−2805.

(12) Liu, L.; Zhao, C.; Xu, J.; Li, Y. Integrated CO_2 capture and photocatalytic conversion by a hybrid adsorbent/photocatalyst material. *Appl. Catal. B: Environmental* **2015**, *179*, 489−499.

(13) Sullivan, I.; Goryachev, A.; Digdaya, I. A.; Li, X.; Atwater, H. A.; Vermaas, D. A.; Xiang, C. Coupling electrochemical CO_2 conversion with CO_2 capture. *Nature Catalysis* **2021**, *4* (11), 952−958.

(14) Li, S.; Ongis, M.; Manzolini, G.; Gallucci, F. Non-thermal plasma-assisted capture and conversion of CO_2. *Chem. Eng. J.* **2021**, *410*, 128335.

(15) Sun, S.; Sun, H.; Guan, S.; Xu, S.; Wu, C. Integrated CO_2 capture and methanation on Ru/CeO_2-MgO combined materials: Morphology effect from CeO_2 support. *Fuel* **2022**, *317*, 123420.

(16) Shao, B.; Hu, G.; Alkebsi, K. A.; Ye, G.; Lin, X.; Du, W.; Hu, J.; Wang, M.; Liu, H.; Qian, F. Heterojunction-redox catalysts of

Fe$_x$Co$_y$Mg$_{10}$CaO for high-temperature CO$_2$ capture and in situ conversion in the context of green manufacturing. *Energy Environ. Sci.* **2021**, *14* (4), 2291−2301.

(17) Wang, G.; Guo, Y.; Yu, J.; Liu, F.; Sun, J.; Wang, X.; Wang, T.; Zhao, C. Ni-CaO dual function materials prepared by different synthetic modes for integrated CO$_2$ capture and conversion. *Chem. Eng. J.* **2022**, *428*, 132110.

(18) Wang, F.; Harindintwali, J. D.; Yuan, Z.; Wang, M.; Wang, F.; Li, S.; Yin, Z.; Huang, L.; Fu, Y.; Li, L. Technologies and perspectives for achieving carbon neutrality. *Innovation* **2021**, *2* (4), 100180.

(19) Hale, T.; Kuramochi, T.; Lang, J.; Yeo, Z. Y.; Smith, S.; Black, R.; Chalkley, P.; Hans, F.; Hay, N.; Höhne, N.; Angel Hsu, C.; Hyslop, a. *Net Zero Tracker.* https://zerotracker.net/#companies-table (accessed 20 Aug 2023).

(20) Braga, A. H.; Vidinha, P.; Rossi, L. M. Hydrogenation of carbon dioxide: From waste to value. *Current Opinion in Green and Sustainable Chemistry* **2020**, *26*, 100386.

(21) Merkouri, L.-P.; Reina, T. R.; Duyar, M. S. Closing the Carbon Cycle with Dual Function Materials. *Energy Fuels* **2021**, *35* (24), 19859−19880.

(22) Sun, H.; Zhang, Y.; Guan, S.; Huang, J.; Wu, C. Direct and highly selective conversion of captured CO$_2$ into methane through integrated carbon capture and utilization over dual functional materials. *J. CO2 Util.* **2020**, *38*, 262−272.

(23) Marafi, M.; Stanislaus, A. Options and processes for spent catalyst handling and utilization. *J. Hazard. Mater.* **2003**, *101* (2), 123−132.

(24) Sun, S.; Lv, Z.; Qiao, Y.; Qin, C.; Xu, S.; Wu, C. Integrated CO$_2$ capture and utilization with CaO-alone for high purity syngas production. *Carbon Capture Science & Technology* **2021**, *1*, 100001.

(25) Fan, J.; Yue, X.; Liu, Y.; Li, D.; Feng, J. An integration system derived from LDHs for CO$_2$ direct capture and photocatalytic coupling reaction. *Chem. Catalysis* **2022**, *2* (3), 531−549.

(26) Yin, H.; Mao, X.; Tang, D.; Xiao, W.; Xing, L.; Zhu, H.; Wang, D.; Sadoway, D. R. Capture and electrochemical conversion of CO$_2$ to value-added carbon and oxygen by molten salt electrolysis. *Energy Environ. Sci.* **2013**, *6* (5), 1538−1545.

(27) Al-Mamoori, A.; Thakkar, H.; Li, X.; Rownaghi, A. A.; Rezaei, F. Development of potassium-and sodium-promoted CaO adsorbents for CO2 capture at high temperatures. *Ind. Eng. Chem. Res.* **2017**, *56* (29), 8292−8300.

(28) Xu, Y.; Donat, F.; Luo, C.; Chen, J.; Kierzkowska, A.; Awais Naeem, M.; Zhang, L.; Muller, C. R. Investigation of K$_2$CO$_3$-modified CaO sorbents for CO$_2$ capture using in-situ X-ray diffraction. *Chem. Eng. J.* **2023**, *453*, 139913.

(29) Tlili, M.; Amor, M. B.; Gabrielli, C.; Joiret, S.; Maurin, G.; Rousseau, P. Characterization of CaCO$_3$ hydrates by micro-Raman spectroscopy. *J. Raman Spectrosc.* **2002**, *33* (1), 10−16.

(30) Kresse, G.; Furthmüller, J. Efficiency of ab-initio total energy calculations for metals and semiconductors using a plane-wave basis set. *Comput. Mater. Sci.* **1996**, *6* (1), 15−50.

(31) Kresse, G.; Furthmüller, J. Efficient iterative schemes for ab initio total-energy calculations using a plane-wave basis set. *Phys. Rev. B* **1996**, *54* (16), 11169.

(32) Blöchl, P. E. Projector augmented-wave method. *Phys. Rev. B* **1994**, *50* (24), 17953.

(33) Monkhorst, H. J.; Pack, J. D. Special points for Brillouin-zone integrations. *Phys. Rev. B* **1976**, *13* (12), 5188.

(34) Perdew, J. P.; Burke, K.; Ernzerhof, M. Generalized gradient approximation made simple. *Phys. Rev. Lett.* **1996**, *77* (18), 3865.

(35) Grimme, S.; Antony, J.; Ehrlich, S.; Krieg, H. A consistent and accurate ab initio parametrization of density functional dispersion correction (DFT-D) for the 94 elements H-Pu. *J. Chem. Phys.* **2010**, *132* (15), 154104.

(36) Grimme, S.; Ehrlich, S.; Goerigk, L. Effect of the damping function in dispersion corrected density functional theory. *J. Comput. Chem.* **2011**, *32* (7), 1456−1465.